Pacific shoreline erosion and accretion patterns controlled by El Niño/Southern Oscillation

Kilian Vos[1], Mitchell D. Harley[1], Ian L. Turner[1], Kristen D. Splinter[1]

[1] Water Research Laboratory, School of Civil and Environmental Engineering, UNSW Sydney, 110 King Street, Manly Vale, NSW 2093, Australia

Corresponding author: Kilian Vos, Water Research Laboratory, School of Civil and Environmental Engineering, UNSW Sydney. Email address: k.vos@unsw.edu.au

In the Pacific Basin, the El Niño/Southern Oscillation (ENSO) is the dominant mode of interannual climate variability, driving substantial changes in oceanographic forcing and impacting Pacific coastlines. Yet, how sandy coasts respond to these basin-scale changes has to date been limited to a few long-term beach monitoring sites, predominantly on developed coasts. Here we use 38 years of Landsat imagery to map shoreline variability around the Pacific Rim and identify coherent patterns of beach erosion and accretion controlled by ENSO. Based on more than 83,000 beach transects covering 8,300km of sandy coastline, we find that approximately one third of all transects experience significant erosion during El Niño phases. The Eastern Pacific is particularly vulnerable to widespread erosion, most notably during the large 1997/1998 El Niño event. In contrast, La Niña events coincide with significant accretion for approximately one quarter of all transects, although substantial erosion is observed in south-east Australia and other localised regions. The observed regional variability in the coastal response to ENSO has important implications for coastal planning and adaptation measures across the Pacific, particularly in light of projected future changes in ENSO amplitude and flavour.

Sandy coasts are estimated to comprise 31% of coastal environments worldwide[1], of which the majority are classified wave-dominated[2]. These coasts are particularly vulnerable to fluctuations in ocean wave energy and water levels, that drive cycles of erosion and accretion at episodic, seasonal, interannual and decadal timescales, impacting adjacent infrastructure and beach habitats. The interannual timescale is of particular interest as it is closely linked to the Earth's climate and its internal modes of climate variability. In a changing climate, a likely change in pattern of these important climate drivers[3,4], coupled with projected changes in storminess[5,6] and rising sea levels, could possibly exacerbate coastal erosion[7] and threaten the future resilience of many coastal communities worldwide[8,9].

In the Pacific Basin, El Niño/Southern Oscillation (ENSO) is the dominant mode of interannual climate variability and has teleconnections with a broad range of atmospheric and oceanic processes along coastal regions[10], influencing nearshore wave climates[11], sea-level anomalies[12] and river discharge[13]. Yet, our understanding of how sandy coasts in the

Pacific respond to these basin-scale changes has to date been limited to a relatively small number (~50 open-coast beaches) of long-term beach monitoring sites, predominantly located along developed coasts in North America, Australia and Japan[14–22], with no observational coverage in Central and South America. Recent innovations in cloud data platforms[23] and remote sensing algorithms[24–26] have opened up the possibility for coastal change to be quantified at unprecedented global scales using satellite imagery. While this approach has been successfully used to identify global long-term trends in shoreline change over several decades[1,27], a major factor that has to-date limited the temporal resolution of satellite-derived coastal observations (including interannual variability) has been the effect of high-frequency tidal fluctuations, requiring the use of satellite composite images averaged over large temporal windows (i.e., annually). However, novel methods for beach slope estimation and tidal correction at the global scale[28] now make it possible to map shoreline changes using individual satellite images (typically every 16 days for each Landsat satellite), significantly increasing the frequency of satellite-derived coastal data[29].

Here, we use individual satellite images to derive shoreline time-series spanning three Landsat missions (1984-2022) along wave-dominated sandy coastlines around the Pacific Basin. We present a detailed overview of the teleconnections between regional patterns of coastal erosion and accretion in the Pacific and ENSO. To further investigate the mechanisms responsible for the observed regional patterns of shoreline variability, we perform a basin-scale analysis of the variations in coastal wave energy flux and sea-level anomalies during the two opposite phases of ENSO. Lastly, we identify temporal patterns of extreme beach erosion associated with major ENSO events over the past 38 years.

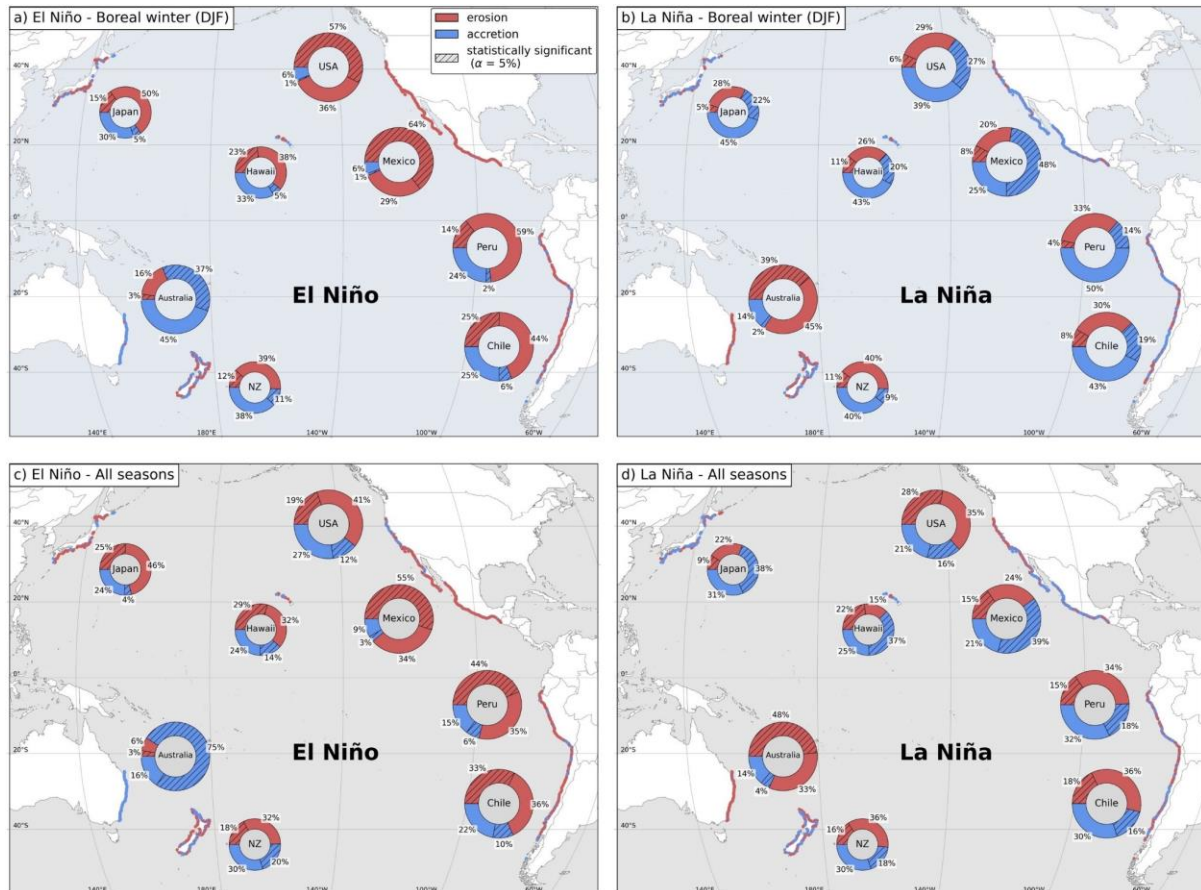**Regional patterns of shoreline response to ENSO**

Wave-dominated sandy beaches across the Pacific were identified and mapped based on the availability of Landsat images and use of the Relative Tidal Range (RTR = Spring Tidal Range/Average Wave Height) to distinguish wave-dominated (RTR<3) from more tide-dominated coasts (Methods, and Supplementary Figs. S2.1). The *CoastSat* toolbox[30] was then used to automatically map the shoreline position on Landsat 5 (1984-2013), Landsat 7 (1999-2022) and Landsat 8 (2013-2022) images, a validation of the satellite-derived shorelines against *in situ* surveys around the Pacific Basin is provided in Supplementary Information (SI) S1. The resulting time-series of shoreline change were tidally-corrected along 100 m-spaced cross-shore transects using a global tide model and a satellite-derived estimate of the average local beach slope[28], amounting to 83,677 beach transects in total across the Pacific (equivalent to 8,367 km of sandy coast, full dataset shown in SI Fig. S2.2).

To investigate the effect of ENSO on interannual shoreline variability, we evaluated anomalies in shoreline position during El Niño and La Niña phases at each transect. The Multivariate ENSO Index (MEI), considered as one of the most complete indices describing ENSO[31] years (comparison of ENSO indices in Supplementary Information S3.1), was used to identify El Niño and La Niña periods during the past 38 years. At each transect, a statistical test (non-parametric Wilcoxon signed rank test) was performed to assess whether the

shoreline positions during each ENSO phase were significantly different (at the 5% significance level) than the long-term average (see Methods and SI S3.3). This test rigorously takes into account the inherent noise of satellite-derived shoreline observations resulting from shoreline detection error (10-15 m, SI S1.1). Also, with strong seasonal shoreline variability evident particularly in the northern hemisphere, where energetic wave conditions primarily occur during the boreal winter (DJF)[32], additional anomaly analyses were carried out for boreal winter shorelines as well as shorelines for all four seasons (see Methods and SI S3.2).

Figure 1 summarizes the regional sandy coastline response to El Niño and La Niña phases for the boreal winter-only shorelines as well as shorelines from all four seasons. Considering the entire Pacific, 70% of all transects indicate beach erosion during El Niño phases, of which 33% are statistically significant in the two analyses (i.e., boreal winter and all seasons). Focusing on the regional variability, the Eastern Pacific (USA, Mexico, Peru, and Chile) is identified as showing a particularly coherent erosion response to El Niño phases, with 50% of transects (boreal winter) showing significant erosion (Fig. 1a). Concurrently, broad accretion is observed during El Niño phases along sandy beaches in south-east Australia, where 75% of transects (all seasons) experience significant beach accretion (Fig. 1c).

By contrast, during La Niña phases, 60% of all transects indicate beach accretion, of which 25% are statistically significant. Positive shoreline anomalies are predominantly found in the Eastern Pacific, while widespread erosion is observed during La Niña phases along south-east Australia (48% of transects experiencing significant erosion for all seasons, Fig. 1d). Along the coasts of smaller island nations where suitable Landsat imagery were available (New Zealand, Japan, and Hawaii), the shoreline data shows a mixed response to ENSO. While the proportion of statistically significant anomalies is not sufficient to infer a coherent regional response at these islands, it can be observed that Hawaii tends to erode during El Niño and accrete during La Niña phases (all seasons), as does Japan.

Fig. 1 | Regional patterns of shoreline response to ENSO along the Pacific Rim. Teleconnections between shoreline variability and ENSO along wave-dominated sandy beaches in the Pacific during the boreal winter season only (**a,b**) and during all four seasons (**c,d**). The negative anomalies are labelled as 'erosion' and positive anomalies as 'accretion'. The pie charts indicate the proportion of transects that experience anomalous erosion (red) or accretion (blue) during El Niño (**a,c**) and La Niña (**b,d**) phases for each region. The proportion of transects along which the anomalies are statistically significant at a 5% significance level (Methods) are hashed.

Changes in oceanographic forcing associated with ENSO

As sandy beaches generally erode in response to energetic waves and/or elevated water levels[7,33,34] and accrete during calmer periods[35,36], the spatial distribution of these two key oceanographic variables were analysed at the same coastal locations as the satellite shoreline analysis. This was undertaken using the ERA5 wave reanalysis and daily sea-level anomalies from satellite altimetry observations (detrended to reduce sea-level rise, see Methods), with both datasets provided at a global scale by the European Centre for Medium-Range Weather Forecasts (ECMWF). Figure 2 shows regional differences in wave energy flux during positive and negative ENSO phases, considering both boreal winter and all seasons. The impact of ENSO on sea-level anomalies across Pacific regions is indicated in Figure 3.

The widespread regional erosion during El Niño phases observed particularly in the Eastern Pacific is consistent with a concurrent increase in wave energy flux in USA and Mexico (22% and 14% increase during boreal winter, respectively) and significant increases (+5 to +10 cm) in sea-level anomalies along the whole Eastern boundary. In Peru and Chile, wave energy flux shows a weak response to El Niño. This likely accounts for the lesser widespread shoreline erosion observed in Peru and Chile (44% and 33% of all transects, all seasons) compared to

4

USA and Mexico (54% and 67%, boreal winter). During La Niña phases, deviations in both wave energy flux and sea-level anomalies generally indicate an inverse response in the Eastern Pacific, consistent with the observed overall positive shoreline anomaly during this phase.

In the Western Pacific, sea-level anomalies are for the most part not-statistically significant. However, the strong and out-of-phase shoreline response to ENSO observed in south-east Australia (Figs. 1c and 1d) is also associated with an increase in wave energy flux (+7%) during La Niña phases and decrease (-6%) during El Niño phases as reported in Figs. 2c and 2d (all seasons). The mixed shoreline response observed along the island nations is likely the result of their widely diverse coastline orientation (SI Fig. S2.2) and subsequent exposure to a multitude of wave sources across the Pacific (e.g., New Zealand and Hawaii being exposed to both Northern and Southern Pacific wave climates). This sensitivity to localized wave exposure and associated coastal response is also evident in several sub-regions (e.g., Baja California, northern Peru).
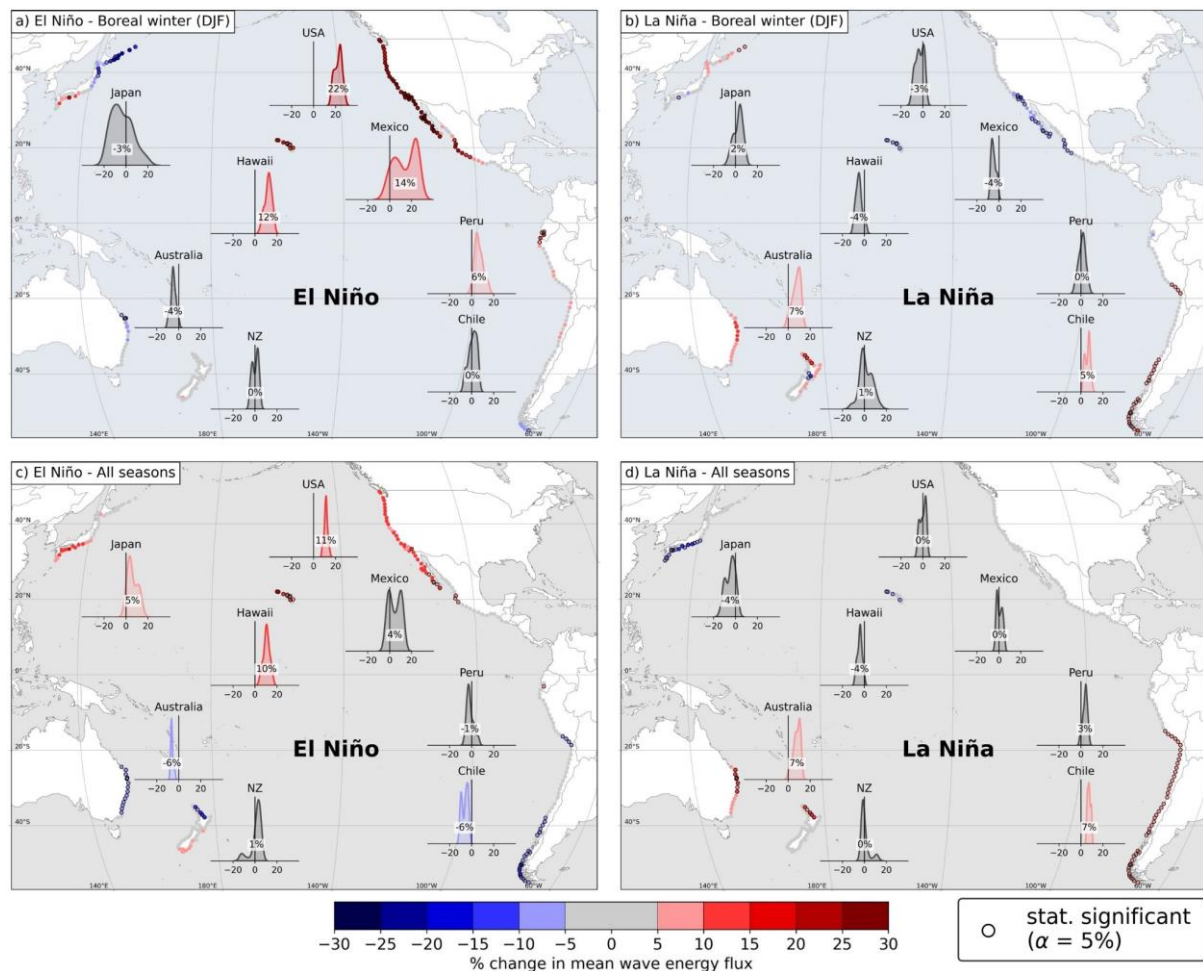
Fig. 2 | Teleconnections between wave energy flux and ENSO phases along the Pacific Rim. The maps show the percentage change in mean wave energy flux during the boreal winter season only (**a**,**b**) and during all four seasons (**c**,**d**) for El Niño (**a**,**c**) and La Niña (**b**,**d**) phases. Anomalies are calculated along a 50 km-grid using ERA5 wave data between 1979-2021 (Methods). The anomalies that are statistically significant at a 5% significance level are outlined with a circle. A probability distribution function (PDF) of all the grid points belonging to each region is plotted as well, the colour of the distribution represents the position of the mean along the colour bar (e.g., grey if the mean of the distribution is between -5 and 5% anomaly).
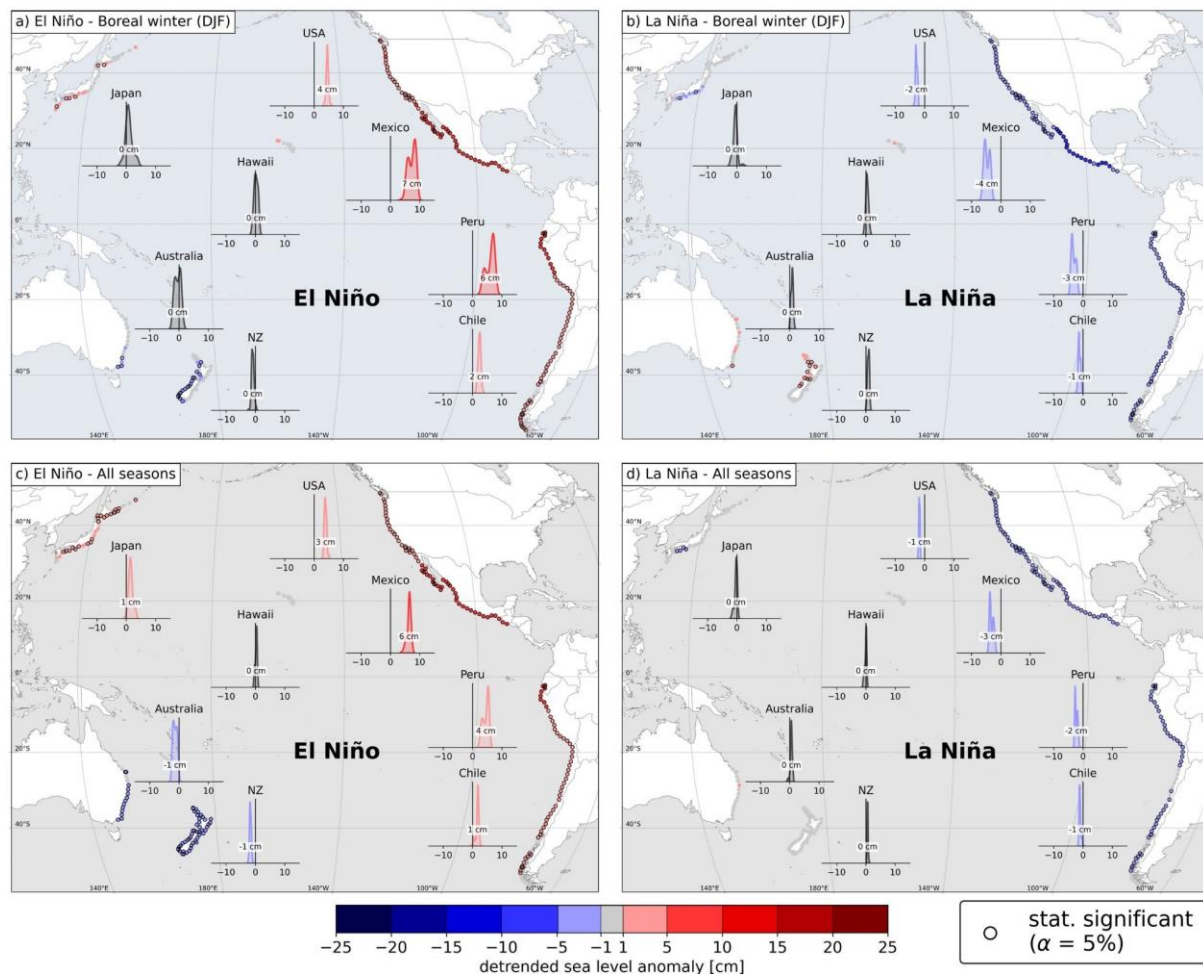
Fig. 3 | Teleconnections between sea-level anomalies and ENSO phases along the Pacific Rim. The maps show differences in detrended sea-level anomalies during the boreal winter season only (**a**,**b**) and during all four seasons (**c**,**d**) for El Niño (**a**,**c**) and La Niña (**b**,**d**) phases calculated along a 50 km-grid using the ECMWF multi-mission altimetry dataset between 1993-2021 (Methods). The anomalies that are statistically significant at a 5% significance level are outlined with a cirlce. A probability distribution function (PDF) of all the grid points belonging to each region is plotted as well, the colour of the distribution represents the position of the mean along the colour bar (e.g., grey if the mean is between -1 and 1 cm anomaly).

==Extreme beach erosion== and links to major ENSO events

In addition to regional patterns in coastal erosion and accretion due to ENSO (Fig. 1), shoreline time-series were analysed to identify extreme beach erosion associated with major ENSO events of the past 38 years. Extreme beach erosion was defined by the lowest 5% of seasonally-averaged shorelines and collated for each region to highlight widespread extreme erosion in either El Niño, La Niña or Neutral years (Methods). This temporal variability in extreme beach erosion is shown for each region in Figure 4.

Overall, the regional pattern is consistent with the more general shoreline erosion and accretion patterns in Figure 1, with extreme beach erosion associated with major El Niño events in the Eastern Pacific and, inversely, major and prolonged La Niña phases in south-east Australia. In the Eastern Pacific, ==this analysis reveals that the 1997/1998 Eastern Pacific (EP) El Niño event was the most erosive over the past 38 years,== during which close to 50% of all

transects experienced widespread extreme erosion across the four regions from USA to Chile (Figs. 4e-h). The 2009/2010 Central Pacific (CP) and 2015/2016 mixed (EP/CP) El Niño events also indicate widespread regional erosion in USA and Mexico, but to a lesser spatial extent than the 1997/1998 EP event. Based on these observations, in USA and Mexico 43% and 57% of the transects, respectively, experienced extreme erosion (i.e., defined as the lowest seasonally-averaged shoreline being below the 5th percentile) during the 1997/1998 event. Comparatively, during the 2009/2010 and 2015/2016 events this number only amounts to 29% and 18%, respectively, for USA, and 22% and 23% for Mexico. In Peru and Chile, the spatial extent of the extreme erosion observed during the 1997/1998 event (~50% of transects) has not been observed since then, with the 2009/2010 and 2015/2016 events not resulting in particularly widespread erosion.

Also apparent in Figure 4 is the role of antecedent conditions on extreme erosion, with observations of persistent erosion in years following major ENSO events. For example, in the Eastern Pacific the 1997/1998 El Niño is followed by a La Niña year, but the percentage of extremely eroded transects in that year remains high as beaches may still be in a slow recovery period. Similarly in Australia, the most widespread erosion (47% of transects experiencing extreme erosion) is observed in 2012/2013, which does not correspond to a major La Niña phase but follows two consecutive years of strong La Niña conditions. This highlights how El Niño and La Niña can trigger prolonged erosion phases on sandy coastlines, as has been observed at local sites using long-term *in situ* data[37]. Future work is needed to clarify the complex lagged responses between oceanic forcing, erosion, and longer-term beach recovery at the Pacific Basin scale.

Fig. 4 | Temporal patterns in regional shoreline erosion between 1984 and 2021. This figure shows the coherent regional shoreline response to major La Niña events (1988/1989, 1999-2001, 2008-2009, 2011-2014 and the ongoing 2021-2022 phase) along the south-eastern Australian coast and major El Niño events (1997/1998, 2009/2010, 2015/2016) along the Eastern Pacific**.** The bar plots show the percentage of transects in each region where the seasonally-averaged shorelines were in the lowest 1% (dark grey) and 1 to 5% (light grey) for each given year in the shoreline record. El Niño years are shown in red and La Niña years in blue, while Neutral years remain grey. **(i)** Time-series of the monthly Multivariate ENSO Index (MEI). El Niño, La Niña and neutral years are defined based on the Oct-Nov-Dec (OND) average of MEI values and a 0.5 standard deviation threshold: El Niño year ($MEI_{OND} > 0.5\sigma_{MEI}$), La Niña years ($MEI_{OND} < -0.5\sigma_{MEI}$), neutral years ($|MEI_{OND}| < 0.5\sigma_{MEI}$).

Regional variability in ENSO and future Pacific coastal response

We have shown how the El Niño/Southern Oscillation causes large regional variability in coastal erosion and accretion along the Pacific Rim. Interannual shoreline response to ENSO is most coherent along the Eastern Pacific and south-east Australia, but with opposite phase. In view of current ENSO projections, which point towards an increase in the frequency of extreme El Niño events[3,38], a shift in their 'flavor'[39] from Eastern Pacific to Central Pacific [40,41], and an increase in frequency of La Niña events[42], our analyses suggest that the Eastern Pacific and south-east Australia emerge as the sectors of the Pacific Rim most susceptible to enhanced ENSO-driven interannual shoreline variability in a warming climate.

Furthermore, the temporal variability in extreme coastal erosion spanning the past 38 years suggest that, along the Eastern Pacific (California to Chile), recent El Niño events with a strong CP component[43–46] (i.e. the 2003/2004, 2009/2010 and 2015/2016 events) have resulted in less widespread erosion compared to the canonical 1997/1998 EP event. This is in line with

the severity of oceanographic forcing during each event, also reported[22], which shows that during the three largest events in the study period, the largest increase in wave energy flux and sea-level anomalies along the Eastern Pacific (California to Chile) occurred during the 1997/1998 event, with relatively weaker oceanographic forcings during the 2015/2016 mixed event and substantially weaker during the 2009/2010 CP event (SI Fig. S5). Future research should focus on understanding the mechanisms by which different types of El Niño influence oceanographic forcing across the oceanic basin and how these may affect open-coast sandy coastlines in a CP-El Niño dominated climate.

Methods

Sandy beaches dataset. A first pass to identify suitable sandy beaches in the Pacific Basin to investigate regional variability controlled by ENSO was undertaken based on two primary criteria: (1) only wave-dominated sandy coastlines (i.e., coastlines primarily controlled by wave, rather than tidal, processes); and (2) the availability of Landsat images for satellite-derived shoreline mapping, due to the inconsistent geographical coverage of the Landsat archive[47].

Wave-dominated coastlines were classified based on the Relative Tidal Range (RTR)[48], calculated here as the ratio between the average deep-water Significant Wave Height, obtained from ERA5 reanalysis[49] and the Spring Tidal Range, obtained from the FES2014 global tide model[50]. Supplementary Information (SI) Fig. S2.1 depicts the spatial distribution of Significant Wave Height (subplot a), Spring Tidal Range (subplot b) and the resulting RTR (subplot c). Coastlines with an RTR < 3 were classified as wave-dominated, while the other coastlines were labelled as tide-modified (RTR = 3-10) or tide-dominated (RTR = 10-50). Regions excluded from this study based on this criterion included north-east Australia, China, Alaska, Canada, and Central America.

Regarding image availability, Landsat images suitable for time-series analysis are categorized as Tier 1 due to their consistent quality through time and across instruments. The availability of Tier 1 Landsat images between 1984 and 2020 (Landsat 5, 7, 8) varies across the Pacific Basin, as shown in SI Fig. S2.1d. For example, islands in the south-west Pacific (including Papua New Guinea and the Philippines) and in the Arctic, as well as the shores of Central America, do not contain sufficient images (minimum set at 600) to achieve continuous monitoring over the 38-year study period. Therefore, these regions were also discarded from the analysis. Based on the two criteria described above, a total of 7 regions were identified as suitable for this analysis: Australia's south-east coast, New Zealand, Chile, Peru, Mexico's west coast, USA's west coast and Japan. For each region, a dataset of sandy beach locations was compiled using the OpenStreetMap database[51] (using the query *natural type* = 'beach' and *surface type* = 'sand') and manually digitized where necessary. The sandy shoreline locations were then used to generate 100 m alongshore-spaced shore-normal transects.

From a first-pass dataset of more than 110,000 beach transects using the two criteria above, a secondary, more-detailed, filtering step was applied to discard transects based on the following conditions:

- Transects where shoreline time-series (see next section on shoreline mapping) contained insufficient data for beach slope estimation (and hence tidal correction). This corresponded to a defined lower limit of 180 shorelines at each transect, or 5 shorelines/year. [75% of the total discarded transects in this second pass]
- Transects where the shoreline time-series indicated a strong linear trend of erosion or accretion (threshold ±3m/year based on [1]), that are likely evidence of non-ENSO influences on the shoreline (e.g. major beach nourishments, tectonic shifts, land subsidence). [10% of discarded transects]
- Transects along small pocket beaches (less than 500 m in length) that may be dominated by cellular beach circulation effects. [5% of discarded transects]
- Transects along high-energy meso-macrotidal beaches (but still classified as wave-dominated) as these require a more sophisticated water level correction for accurate shoreline mapping[52]. These include sandy beaches along the Oregon and Washington coasts as well as localised stretches of coastline along New Zealand's West coast. [10% of discarded transects]

This amounted to a final dataset of 83,677 beach transects (74% of the first-pass dataset) across the seven regions used for the ENSO anomaly analysis. SI Fig. S2.2 illustrates the spatial extent of this dataset, including the number of transects and their orientation for each region.

Satellite-derived shorelines. The CoastSat open-source Python toolkit[30] (available at https://github.com/kvos/CoastSat) was used to extract Landsat images between 1984 and 2022 at each beach (using the Google Earth Engine API[23]) and automatically map the position of the shoreline on each image. Briefly, CoastSat's detection algorithm combines a supervised image classification and a sub-pixel resolution border segmentation to map the position of the instantaneous boundary between sand and water with a shoreline accuracy of 10-15 m[26] (see comparison with *in situ* shoreline data in SI Fig. S1.1). A noteworthy improvement in this study over the default CoastSat toolbox was to create a more generalised classifier (originally trained on 5 Australian beaches) using tens of images from sites across the 7 regions, including Chilean black sand beaches, Chilean bright sand Atacama Desert beaches, Mexican tropical beaches as well as Japanese snow-covered beaches. Thus, this extended classifier was capable of identifying sandy pixels at a wide range of coastal environments, making the shoreline detection more robust at the Pacific-basin scale. The intersection of the two-dimensional shorelines with the shore-normal transects were subsequently calculated to produce time-series of cross-shore shoreline change at each transect.

Tidal correction. Since every satellite image was taken at a different stage of the tide, the time-series of shoreline change obtained in the previous step were tidally-corrected to remove high-frequency shoreline changes related to tidal variations. To do this, water levels

at the time of image acquisition and an estimate of the beach slope are necessary. Since obtaining measured water levels for each beach at the basin scale is not plausible, modelled tides from the FES2014 global tide model[50] were used. The beach slope along each transect was then estimated from the satellite-derived shorelines and corresponding tide levels using a method described in [28] (available at https://github.com/kvos/CoastSat.slope). This technique applies a frequency domain analysis to the shoreline time-series to find the optimum slope that, when used for tidal correction, minimises high-frequency tidal fluctuations relative to lower-frequency erosion/accretion signals.

Validation of satellite-derived shorelines. The accuracy of the satellite-derived shorelines obtained with *CoastSat* has been evaluated in two previous studies [26,52], and to date, the toolbox has been used in a number of recent publications by other authors to extract shoreline observations along open-coast sandy beaches worldwide[53–59]. In Supplementary Information S1, we have compiled all the *in situ* long-term shoreline datasets available along the Pacific Rim:

- 16 years at Torrey Pines (San Diego, USA), publicly available and described in [60]
- 18 years at Ocean Beach (San Francisco, USA), described in [61,62]
- 34 years at Narrabeen-Collaroy (Australia), publicly available and described in [63]
- 10 years at Moruya (Australia), described in [64]
- 20 years at Tairua Beach (New Zealand), described in [65,66]

The comparison between *in situ* surveyed data and satellite-derived shorelines is presented in SI Fig. S1.1 and indicates a standard deviation error of the order of 10 m across more than 10,000 *in situ* survey points and demonstrates how monthly-averaged satellite-derived shorelines are capable of capturing interannual shoreline variability at these 5 sites. Additionally, the range of coastal environments (characterised by tidal range, incident wave energy, and beach-face slope) captured by the 5 validation sites is compared to the variability of the entire dataset in SI Fig S2.3. It indicates a good coverage of the parameter space as the dataset was restricted to microtidal wave-dominated beaches. It is acknowledged however, that the validation sites do not include beaches that are optically different (e.g., black sand beaches) or composed of coarser sediment (e.g., gravel).

Anomalies in shoreline position during ENSO phases. To evaluate the effect of ENSO on shoreline variability, monthly-averaged shoreline positions during El Niño and La Niña phases were compared to the long-term average shoreline position along each transect. El Niño and La Niña phases were defined as the periods of time during which the intensity of the Multivariate ENSO Index[31] (MEI) was stronger than half of its standard deviation, in a similar way to [45]. Monthly-averaged shoreline positions were then computed to homogenise the temporal resolution of the satellite-derived time-series, and avoid a potential bias caused by the high density of shorelines over the more recent part of the record. To test whether the shorelines during the El Niño/La Niña phases are significantly wider or narrower than the long-term average, a statistical test was used, a Wilcoxon signed-rank test — the distribution-free

equivalent of a one-sample t-test[67]. The resulting p-value indicates the probability of the mean of the population being greater or less than (one-tailed) the long-term average. Distributions with a mean greater (less) than the long-term average were labelled as 'erosion' ('accretion'). The statistical test was repeated for both ENSO phases and evaluated for the boreal winter (DJF) anomalies as well as anomalies from all seasons, generating four p-values for each transect, as presented in the four subplots of Figure 1 in the main manuscript. The two separate anomaly analyses, over DJF-only shorelines and all seasons, were performed to address the strong seasonality in shoreline variability of the northern hemisphere[32], and avoid potential biases that may emerge when ENSO is locked in the seasonal cycle (further discussion on this in SI S3.2). The statistical robustness of this analysis is discussed in details and validated in Supplementary Information S4.

Supplementary Figures S3.3.1 and S3.3.2 show the step-by-step procedure along two different transects located respectively along Ocean Beach (San Francisco, USA) and Narrabeen (Sydney, Australia). The monthly-averaged shoreline positions (subplot a), ENSO index (subplot b), shoreline seasonal variability (subplot c), and the shoreline ENSO anomalies during both phases for all seasons (subplot d) and DJF-only (subplot e) are presented in the figures. These two examples illustrate the importance of considering the DJF period only for seasonally-dominated northern hemisphere beaches like Ocean Beach, where the ENSO anomalies are more pronounced during the boreal winter (DJF), while at a southern hemisphere beach with no apparent seasonality such as Narrabeen, the anomalies are evident when shorelines from all four seasons are considered. As *in situ* data is available at these two sites, the same composite analysis is also performed on the *in situ* record in SI Figs. S3.3.3 and S3.3.4. This analysis demonstrates that the same anomalies and statistical significance found in the satellite-derived time-series are obtained using the *in situ* record, providing further support as to the robustness of the Pacific-wide shoreline analyses.

Anomalies in wave energy flux during ENSO phases. A similar analysis was performed to quantify the effect of ENSO on wave energy flux around the Pacific (Fig. 2). Six-hourly time-series of significant wave height and mean wave period (1984-2022) from the 50 km-resolution ECMWF ERA5 reanalysis[49] were used to calculate wave energy flux in watts per metre of wave front:

$$P = \frac{\rho g^2 {H_s}^2 T}{64\pi}$$

where $\rho = 1025$ kg/m^3, g is the gravitational constant, H_s significant wave height and T mean wave period. An example of wave energy flux time-series at the closest grid point to Ocean Beach (San Francisco, USA) is shown in SI Fig. S3.4. To maintain the same timescale as the satellite observations, the six-hourly wave time-series were monthly averaged and the statistical significance of the observed deviations from the long-term average wave energy flux during both ENSO phases was evaluated with a Wilcoxon signed-rank test, as described above and illustrated step-by-step in SI S3.4.

Sea-level anomalies during ENSO phases. Time-series of daily sea-level anomalies based on satellite altimetry provided by ECMWF and Copernicus Climate Change Service between 1993 and 2022, extracted on the same grid as the wave data, were used to investigate the influence of ENSO on sea level anomalies. The time-series of sea-level anomalies were detrended to reduce any sea-level-rise signal and, as in the previous analysis, the time-series were monthly averaged. An example of sea-level anomaly time-series at the closest grid point to Ocean Beach (San Francisco, USA) and its step-by-step analysis is provided in SI Fig. S3.5. As per above, the statistical significance of the observed differences in sea level anomalies was also evaluated with a Wilcoxon signed-rank test.

Regional extreme beach erosion. Seasonally-averaged time-series of shoreline variability along each transect were first divided into yearly bins, defined from 1 August to 31 July. For each yearly bin, the most eroded datapoint was selected and compared to the lowest 1% and 5% shoreline positions in the record (i.e., 1st and 5th percentiles). The percentage of transects in each of the seven regions that falls below these percentiles is reported in Figure 4.

To classify El Niño, La Niña or Neutral years, the same approach as in [68] was used. The average MEI value during October-November-December (OND) is first calculated, which are the months over which ENSO is known to peak [69], and compared to half a standard deviation of the MEI to classify each year into an El Niño year ($MEI_{OND} > 0.5\sigma_{MEI}$), La Niña year ($MEI_{OND} < -0.5\sigma_{MEI}$) or neutral year ($|MEI_{OND}| < 0.5\sigma_{MEI}$). The MEI_{OND} averaged are plotted in Figure 4i, while El Niño, La Niña and neutral years are colour-coded in the rest of Figure 4.

Corresponding Author

Correspondence and requests for materials should be addressed to Kilian Vos (k.vos@unsw.edu.au).

Author Contributions

K.V., M.H.D., I.L.T. and K.D.S. devised the study, designed the figures and wrote the manuscript. K.V. processed the data (shorelines, waves, and sea level anomalies) and performed the analysis. All authors discussed the results and reviewed the manuscript. M.H.D., I.L.T. and K.D.S. jointly supervised this work.

Data Availability

The full satellite-derived shoreline dataset generated and analysed in the current study is available in the following Zenodo data repository: https://doi.org/10.5281/zenodo.4760144. The data is also displayed on an interactive web portal at http://coastsat.wrl.unsw.edu.au/.

Code Availability

The source code to map satellite-derived shorelines from Landsat imagery (CoastSat) is available at https://doi.org/10.5281/zenodo.2779293. The source code to estimate beach slopes from satellite-derived shorelines and modelled tides (CoastSat.slope) is available at https://doi.org/10.5281/zenodo.3872442.

References

1.   Luijendijk, A. *et al.* The State of the World's Beaches. *Sci. Rep.* 1–11 (2018) doi:10.1038/s41598-018-24630-6.

2.   Nyberg, B. & Howell, J. A. Global distribution of modern shallow marine shorelines. Implications for exploration and reservoir analogue studies. *Mar. Pet. Geol.* **71**, 83–104 (2016).

3.   Cai, W. *et al.* Increasing frequency of extreme El Niño events due to greenhouse warming. *Nat. Clim. Chang.* **4**, 111–116 (2014).

4.   Woollings, T. & Blackburn, M. The north Atlantic jet stream under climate change and its relation to the NAO and EA patterns. *J. Clim.* **25**, 886–902 (2012).

5.   Reguero, B. G., Losada, I. J. & Méndez, F. J. A recent increase in global wave power as a consequence of oceanic warming. *Nat. Commun.* **10**, 1–14 (2019).

6.   Mentaschi, L., Vousdoukas, M. I., Voukouvalas, E., Dosio, A. & Feyen, L. Global changes of extreme coastal wave energy fluxes triggered by intensified teleconnection patterns. *Geophys. Res. Lett.* **44**, 2416–2426 (2017).

7.   Theuerkauf, E. J., Rodriguez, A. B., Fegley, S. R. & Luettich, R. A. Sea level anomalies exacerbate beach erosion. *Geophys. Res. Lett.* **41**, 5139–5147 (2014).

8.   Ranasinghe, R. Assessing climate change impacts on open sandy coasts: A review. *Earth-Science Reviews* (2016) doi:10.1016/j.earscirev.2016.07.011.

9.   Li, N., Yamazaki, Y., Roeber, V., Cheung, K. F. & Chock, G. Probabilistic mapping of storm-induced coastal inundation for climate change adaptation. *Coast. Eng.* **133**, 126–141 (2018).

10.   Troup, A. J. The 'southern oscillation'. *Q. J. R. Meteorol. Soc.* **91**, 490–506 (1965).

11.   Odériz, I., Silva, R., Mortlock, T. R. & Mori, N. ENSO Impacts on Global Wave Climate and Potential Coastal Hazards. *J. Geophys. Res. Ocean.* (2020) doi:10.1029/2020jc016464.

12.   White, N. J. *et al.* Australian sea levels-Trends, regional variability and influencing factors. *Earth-Science Reviews* vol. 136 155–174 (2014).

13.   Ward, P. J., Beets, W., Bouwer, L. M., Aerts, J. C. J. H. & Renssen, H. Sensitivity of river discharge to ENSO. *Geophys. Res. Lett.* **37**, 1–6 (2010).

14.   Vidal-Ruiz, J. A. & Ruiz de Alegría-Arzaburu, A. Variability of sandbar morphometrics over three seasonal cycles on a single-barred beach. *Geomorphology* **333**, 61–72 (2019).

15.   Peterson, C. D., Jackson, P. L., O'Neil, D. J., Rosenfeld, C. L. & Kimerling, A. J. Littoral Cell Response to Interannual Climatic Forcing 1983-1987 on the Central Oregon Coast, USA. *J. Coast. Res.* **6**, 87–110 (1990).

16.   Barnard, P. L. *et al.* The impact of the 2009-10 El Niño Modoki on U.S. West Coast beaches. *Geophys. Res. Lett.* **38**, 1–7 (2011).

17.   Barnard, P. L. *et al.* Extreme oceanographic forcing and coastal response due to the 2015-2016 El Niño. *Nat. Commun.* **8**, (2017).

18.   Kuriyama, Y., Banno, M. & Suzuki, T. Linkages among interannual variations of shoreline, wave and climate at Hasaki, Japan. *Geophys. Res. Lett.* **39**, 2–5 (2012).

19.   Phinn, S. R. & Hastings, P. A. Southern Oscillation Influences on the Gold Coast's Summer Wave Climate. *J. Coast. Res.* **11**, 946–958 (1995).

20.   Ranasinghe, R., McLoughlin, R., Short, A. & Symonds, G. The Southern Oscillation Index, wave climate, and beach rotation. *Mar. Geol.* **204**, 273–287 (2004).

21.   Barnard, P. L. *et al.* Coastal vulnerability across the Pacific dominated by El Niño/Southern Oscillation. *Nat. Geosci.* **8**, 801–807 (2015).

22.   Young, A. P. *et al.* Southern California Coastal Response to the 2015–2016 El Niño. *J. Geophys. Res. Earth Surf.* **123**, 3069–3083 (2018).

23.   Gorelick, N. *et al.* Google Earth Engine: Planetary-scale geospatial analysis for everyone. *Remote Sens. Environ.* **202**, 18–27 (2017).

24.   Pardo-Pascual, J. E., Almonacid-Caballer, J., Ruiz, L. A. & Palomar-Vázquez, J. Automatic extraction of shorelines from Landsat TM and ETM+ multi-temporal images with subpixel precision. *Remote Sens. Environ.* **123**, 1–11 (2012).

25.   Hagenaars, G., de Vries, S., Luijendijk, A. P., de Boer, W. P. & Reniers, A. J. H. M. On the accuracy of automated shoreline detection derived from satellite imagery: A case study of the sand motor mega-scale nourishment. *Coast. Eng.* **133**, 113–125 (2018).

26.   Vos, K., Harley, M. D., Splinter, K. D., Simmons, J. A. & Turner, I. L. Sub-annual to multi-decadal shoreline variability from publicly available satellite imagery. *Coast. Eng.* **150**, 160–

174 (2019).

27. Mentaschi, L., Vousdoukas, M. I., Pekel, J.-F., Voukouvalas, E. & Feyen, L. Global long-term observations of coastal erosion and accretion. *Sci. Rep.* **8**, 12876 (2018).

28. Vos, K., Harley, M. D., Splinter, K. D., Walker, A. & Turner, I. L. Beach Slopes From Satellite-Derived Shorelines. *Geophys. Res. Lett.* **47**, (2020).

29. Castelle, B., Ritz, A., Marieu, V., Nicolae Lerma, A. & Vandenhove, M. Primary drivers of multidecadal spatial and temporal patterns of shoreline change derived from optical satellite imagery. *Geomorphology* **413**, 108360 (2022).

30. Vos, K., Splinter, K. D., Harley, M. D., Simmons, J. A. & Turner, I. L. CoastSat: A Google Earth Engine-enabled Python toolkit to extract shorelines from publicly available satellite imagery. *Environ. Model. Softw.* **122**, 104528 (2019).

31. Wolter, K. & Timlin, M. S. El Niño/Southern Oscillation behaviour since 1871 as diagnosed in an extended multivariate ENSO index (MEI.ext). *Int. J. Climatol.* **31**, 1074–1087 (2011).

32. Young, I. R. Seasonal variability of the global ocean wind and wave climate. *Int. J. Climatol.* **19**, 931–950 (1999).

33. Russell, P. E. Mechanisms for beach erosion during storms. *Cont. Shelf Res* **13**, 1243–1265 (1993).

34. Masselink, G. *et al.* Extreme wave activity during 2013/2014 winter and morphological impacts along the Atlantic coast of Europe. *Geophys. Res. Lett.* 2135–2143 (2016) doi:10.1002/2015GL067492.Received.

35. Phillips, M. S., Harley, M. D., Turner, I. L., Splinter, K. D. & Cox, R. J. Shoreline recovery on wave-dominated sandy coastlines: the role of sandbar morphodynamics and nearshore wave parameters. *Mar. Geol.* **385**, 146–159 (2017).

36. Davidson, M. A., Turner, I. L., Splinter, K. D. & Harley, M. D. Annual prediction of shoreline erosion and subsequent recovery. *Coast. Eng.* **130**, 14–25 (2017).

37. Thom, B. G. & Hall, W. Behaviour of beach profiles during accretion and erosion dominated periods. *Earth Surf. Process. Landforms* **16**, 113–127 (1991).

38. Wang, G. *et al.* Continued increase of extreme El Ninõ frequency long after 1.5 C warming stabilization. *Nat. Clim. Chang.* **7**, 568–572 (2017).

39. Capotondi, A. *et al.* Understanding ENSO Diversity. *Bull. Am. Meteorol. Soc.* **96**, 921–938 (2014).

40. Yeh, S. W. *et al.* El Niño in a changing climate. *Nature* **461**, 511–514 (2009).

41. Freund, M. B. *et al.* Higher frequency of Central Pacific El Niño events in recent decades relative to past centuries. *Nat. Geosci.* **12**, 450–455 (2019).

42. Cai, W. *et al.* Increased frequency of extreme La Niña events under greenhouse warming. *Nat. Clim. Chang.* **5**, 132–137 (2015).

43. Ashok, K., Behera, S. K., Rao, S. A., Weng, H. & Yamagata, T. El Niño Modoki and its possible teleconnection. *J. Geophys. Res. Ocean.* **112**, (2007).

44. Kao, H. Y. & Yu, J. Y. Contrasting Eastern-Pacific and Central-Pacific types of ENSO. *J. Clim.* **22**, 615–632 (2009).

45. Santoso, A., Mcphaden, M. J. & Cai, W. The Defining Characteristics of ENSO Extremes and the Strong 2015/2016 El Niño. *Reviews of Geophysics* vol. 55 1079–1129 (2017).

46. Paek, H., Yu, J. Y. & Qian, C. Why were the 2015/2016 and 1997/1998 extreme El Niños different? *Geophys. Res. Lett.* **44**, 1848–1856 (2017).

47. Wulder, M. A. *et al.* The global Landsat archive: Status, consolidation, and direction. *Remote Sens. Environ.* **185**, 271–283 (2016).

48. Masselink, G. & Short, A. D. The effect of tide range on beach morphodynamics and morphology: a conceptual beach model. *J. Coast. Res.* **9**, 785–800 (1993).

49. Hersbach, H. *et al.* The ERA5 global reanalysis. *Q. J. R. Meteorol. Soc.* **146**, 1999–2049 (2020).

50. Carrere, L., Lyard, F., Cancet, M., Guillot, A. & Picot, N. FES 2014, a new tidal model—Validation results and perspectives for improvements. in *Proceedings of the ESA living planet symposium* 9–13 (2016). doi:https://www.aviso.altimetry.fr/.

51. OSM. OpenStreetMap contributers: Planet dump retrieved from https://planet.osm.org. (2017).

52. Castelle, B. *et al.* Satellite-derived shoreline detection at a high-energy meso-macrotidal beach. *Geomorphology* 107707 (2021) doi:10.1016/j.geomorph.2021.107707.

53. Cuttler, M. V. W. *et al.* Interannual Response of Reef Islands to Climate-Driven Variations in Water Level and Wave Climate. *Remote Sens. 2020, Vol. 12, Page 4089* **12**, 4089 (2020).

54. Lawson, S. K. *et al.* Morphodynamics and Evolution of Estuarine Sandspits along the Bight of Benin Coast, West Africa. *Water 2021, Vol. 13, Page 2977* **13**, 2977 (2021).

55. Nourdi, N. F. *et al.* Seasonal to decadal scale shoreline changes along the Cameroonian coastline, Bay of Bonny (1986 to 2020). *Reg. Stud. Mar. Sci.* **45**, 101798 (2021).

56. Taveneau, A. *et al.* Observing and predicting coastal erosion at the langue de barbarie sand spit around saint louis (Senegal, west africa) through satellite-derived digital elevation model and shoreline. *Remote Sens.* **13**, 2454 (2021).

57. Adebisi, N., Balogun, A. L., Mahdianpari, M. & Min, T. H. Assessing the impacts of rising sea level on coastal morpho-dynamics with automated high-frequency shoreline mapping using multi-sensor optical satellites. *Remote Sens.* **13**, 3587 (2021).

58. Sokolewicz, M., Bergsma, L., Schemmekes, L., Nguyen, H. & Boersen, S. USE OF REMOTE SENSING TECHNIQUES AND NUMERICAL MODELLING TO PREDICT COASTAL EROSION IN VIETNAM. *Coast. Eng. Proc.* 65 (2020) doi:10.9753/icce.v36v.papers.65.

59. Balouin, Y., Bourrin, F., Meslard, F., Palvadeau, E. & Robin, N. Assessing the Role of Storm

Waves and River Discharge on Sediment Bypassing Mechanisms at the Têt River Mouth in the Mediterranean (Southeast France). *J. Coast. Res.* **95**, 351–355 (2020).

60.   Ludka, B. C. *et al.* Sixteen years of bathymetry and waves at San Diego Beaches. *Sci. Data* **6**, 161 (2019).

61.   Hansen, J. E. & Barnard, P. L. Sub-weekly to interannual variability of a high-energy shoreline. *Coast. Eng.* **57**, 959–972 (2010).

62.   Barnard, P. L., Hansen, J. E. & Erikson, L. H. Synthesis Study of an Erosion Hot Spot, Ocean Beach, California. *J. Coast. Res.* **28**, 903–922 (2012).

63.   Turner, I. L. *et al.* A multi-decade dataset of monthly beach profile surveys and inshore wave forcing at Narrabeen, Australia. *Sci. data* **3**, 160024 (2016).

64.   Bracs, M. A., Turner, I. L., Splinter, K. D., Short, A. D. & Mortlock, T. R. Synchronised patterns of erosion and deposition observed at two beaches. *Mar. Geol.* **380**, 196–204 (2016).

65.   Van de Lageweg, W. I., Bryan, K. R., Coco, G. & Ruessink, B. G. Observations of shoreline-sandbar coupling on an embayed beach. *Mar. Geol.* **344**, 101–114 (2013).

66.   Blossier, B., Bryan, K. R., Daly, C. J. & Winter, C. Shore and bar cross-shore migration, rotation, and breathing processes at an embayed beach. *J. Geophys. Res. Earth Surf.* **122**, 1745–1770 (2017).

67.   Meek, G. E., Ozgur, C. & Dunning, K. Comparison of the t vs. Wilcoxon Signed-Rank test for likert scale data and small samples. *J. Mod. Appl. Stat. Methods* **6**, 91–106 (2007).

68.   Izumo, T. *et al.* Influence of the state of the Indian Ocean Dipole on the following years El Nĩo. *Nat. Geosci.* **3**, 168–172 (2010).

69.   Choi, K. Y., Vecchi, G. A. & Wittenberg, A. T. ENSO transition, duration, and amplitude asymmetries: Role of the nonlinear wind stress coupling in a conceptual model. *J. Clim.* **26**, 9462–9476 (2013).